REPORT DOCUMENTATION PAGE

AFRL-SR-AR-TR-02-
0824

1. AGENCY USE ONLY *(Leave blank)*	2. REPORT DATE	3. REPORT TYPE AND DATES COVERED
	26-AUG-2002	FINAL (01-MAR-2001 TO 31-MAY-2002)

4. TITLE AND SUBTITLE
A MICROSTRUCTURE TESTING AND ANALYSIS LABORATORY

5. FUNDING NUMBERS
F49620-01-1-0245

6. AUTHOR(S)
THOMAS SIEGMUND

7. PERFORMING ORGANIZATION NAME(S) AND ADDRESS(ES)
SCHOOL OF MECHANICAL ENGINEERING
PURDUE UNIVERSITY
1288 MECHANICAL ENGINEERING BUILDING
WEST LAFAYETTE, IN 47907-1288

8. PERFORMING ORGANIZATION REPORT NUMBER

9. SPONSORING/MONITORING AGENCY NAME(S) AND ADDRESS(ES)
AIR FORCE OFFICE OF SCIENTIFIC RESEARCH
4015 WILSON BOULVARD
ARLINGTON, VA 222043

10. SPONSORING/MONITORING AGENCY REPORT NUMBER

11. SUPPLEMENTARY NOTES

12a. DISTRIBUTION AVAILABILITY STATEMENT

Approved for public release;
distribution unlimited.

20021015 079

13. ABSTRACT *(Maximum 200 words)*

The "Microstructure Testing and Analysis Laboratory" is a new facility for the mechanical testing of small specimens, soft material, and small structures. The main components of the laboratory are a low force electrodynamically actuated test frame for axial/torsion and combined loading, a digital image correlation system for the measurement of displacement fields, and a stereovision system for investigations of fracture surface

The facilities have been used successfully in research projects on carbon-carbon composites, and in investigations of porous polymeric materials, as well as for projects in a graduate course on "Micromechanics of Materials." In all experiments performed so far the experimental facilities have performed satisfactory.

14. SUBJECT TERMS	15. NUMBER OF PAGES
	29
	16. PRICE CODE

17. SECURITY CLASSIFICATION OF REPORT	18. SECURITY CLASSIFICATION OF THIS PAGE	19. SECURITY CLASSIFICATION OF ABSTRACT	20. LIMITATION OF ABSTRACT
UNCLASSIFIED	UNCLASSIFIED	UNCLASSIFIED	

A MICROSTRUCTURE TESTING AND ANALYSIS LABORATORY

FINAL REPORT

AUGUST 2002

Thomas Siegmund
Phone: 765 494 9766
Fax: 765 494 0539
Email: siegmund@ecn.purdue.edu

School of Mechanical Engineering
Purdue University
1288 Mechanical Engineering Building
West Lafayette, IN 47907-1288

1. SUMMARY

The "Microstructure Testing and Analysis Laboratory" is a new facility for the mechanical testing of small specimens, soft material, and small structures. The main components of the laboratory are a low force electrodynamically actuated test frame for axial/torsion and combined loading, a digital image correlation system for the measurement of displacement fields, and a stereovision system for investigations of fracture surfaces.

The facilities have been used successfully in research projects on carbon-carbon composites, and in investigations of porous polymeric materials, as well as for projects in a graduate course on "Micromechanics of Materials." In all experiments performed so far the experimental facilities have performed satisfactory.

2. DESCRIPTION OF FACILITY

2.1 Location

The "Microstructure Testing and Analysis Laboratory" is located in the School of Mechanical Engineering, Purdue University, West Lafayette, IN 47907, Potter Building, Room B2; and can be reached at the phone number 765 494-1866.

2.2 Low Force Test Frame

To fulfill requirements for material testing at low forces and high force and displacement resolution experiments on small-scale specimens and structures a commercial micro-force testing system was purchased from EnduraTEC Systems Corporation[1]. This system is the electro-dynamic test system ELF 3200.

The test system is depicted in Figure 1. It consists of a three-column frame to which both axial as well as torsion actuators are attached via a crossbar. The system allows for tests of monotonic and cyclic tension/compression, monotonic and cyclic torsion, as well as for combined axial/torsion loading.

The test system is controlled by a PC and uses the software package "WinTest" from EnduraTec. A screen shot of the control system is provided in Figure 2. Two PC boards are included in the equipment, a conditioner/controller board and a two-channel conditioner board. Three transducer packages are available, and Table 1 summarizes the rating of the transducers, while Table 2 describes the possible combinations of data acquisition channels.

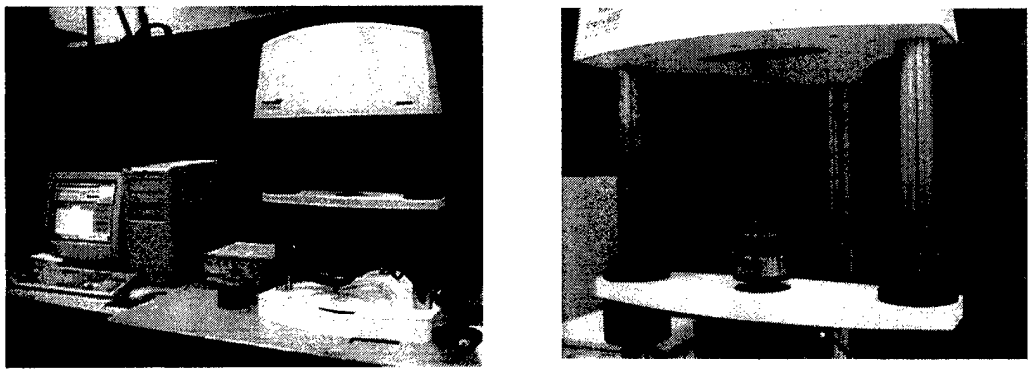

Figure 1: (a) The ELF 3200 Test Frame and the PC used to control the system; (b) Close-up of torsion test set-up.

[1] EnduraTEC can be contacted by mail at 5610 Rowland Road, Minnetonka, Minnesota 55343; via phone and fax at 810 954 1083 and 810 954 1271.

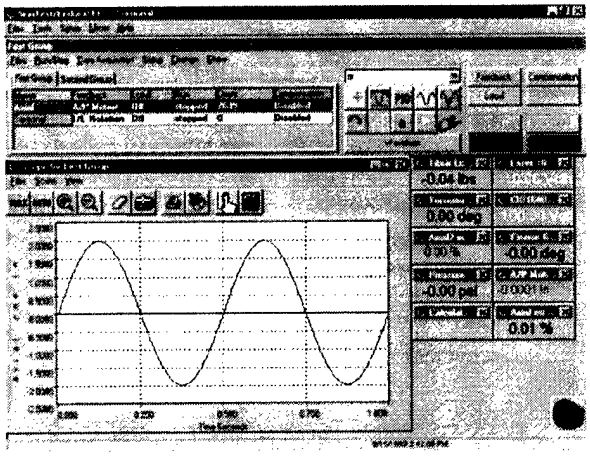

Figure 2: Screen shot of WinTest software.

Transducer	Load range	Load resolution	Displacement Range	Displacement Resolution
Axial #1	±450N	0.01 N	±6.35 mm	0.5 µm
Axial #2	±10 N	0.001 N	±50 µm	10 nm
Torsion	±3.1Nm	0.001 Nm	Multi turn	

Table 1: Transducers for the ELF 3200

	Project File (1)	Project File (2)	Project File (3)
PCI	Displacement ±6.35 mm	Displacement ±6.35 mm	Displacement ±6.35 mm
PCI	Load ±450N	Load ±450N	Displacement ±50 µm
PCI	Load ±10 N	Displacement ±50 µm	Load ±10 N
PCI	Torque ±3.1Nm	Load ±10 N	Torque ±3.1Nm
PC Board Direct	Twist Multi turn	Twist Multi turn	Twist

Table 2: Data acquisition channel availability with the ELF 3200 system

The two sets of axial transducers can be combined with each other such that e.g. experiments with ±6.35 mm displacement range under load resolution of 0.001 N, experiments with ±450N under 10 nm are possible. The main features of the proposed equipment – separating it from conventional mechanical testing equipment – are the electro-dynamic actuators. The electro-dynamic actuators have the advantages over DC and piezo drivers in offering a good combination of frequency and speed ranges as well as attainable stroke. The bearingless actuators make the system virtually maintenance-free and will allow for a lifetime of the equipment into the multi-billion life cycles.

Future expansions of the test system are possible by including additional linear actuators for biaxial/triaxial loading, hot/cold environmental chambers and chemical environments for corrosion testing.

2.3 Digital Image Correlation System

A digital image correlation system was purchased from Correlated Solutions Inc.[2]. This system consists of a digital camera, Fig. 3a, a telecentric lens, Fig. 3b, a PC capture board and data acquisition system, and a digital image correlation software program, VIC2D.

The digital camera is a model QIMAGING Retiga 1300 b/w from Quantitative Image Corp[3]. It possesses a CCD pixel size of 6.7 x 6.7 μm in an array of 1300 x 1300 pixels, and is connected via a digital interface (IEEE 1394 FireWire) to a PC based image system.

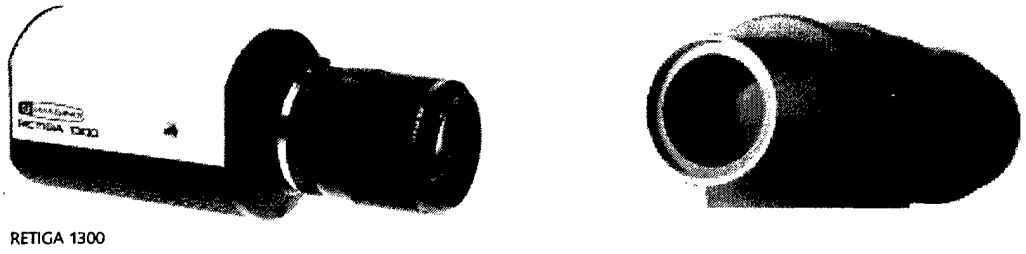

(a) (b)

Figure 3: (a) Retiga digital camera, (b) telecentric lens system.

Furthermore, a data capture board for load and displacements signals from the ELF 3200 system is available such that the experiments conducted in the test frame can be synchronized with the image acquisition.

The telecentric lens is a Xenoplan 1:1 from Schneider Optics Inc[4]. It possesses an object size of 8.8 × 6.6 mm, a working distance of 47±3 mm without any changes in lens magnification, and allows for imaging with a maximum of 1 μm of distortion of the image plane.

The digital imaging system VIC2D from Correlated Solutions compares consecutive image taken during the test. It uses the change in surface characteristics as the specimen is affected by the mechanical stresses imposed upon it to determine

[2] Correlated Solutions, Inc., 952 Sunset Blvd., West Columbia, SC 29169; phone 803 926-7272 and fax 803 926-7221.
[3] Quantitative Imaging Corp., 8081 Lougheed Highway, Burnaby, British Columbia, Canada V5A 1W9; phone 604 708 5061 and fax 604 708 5081.
[4] Schneider Optics Inc., 285 Oser Ave., Hauppauge, NY 11788, phone 631 761 5000 and fax 631 761 5090.

displacement and strain fields. Figure 4 depicts a screen shot of the user interface of the VIC2D program.

Various methods for the preparation of appropriate speckle patterns on specimen surfaces have been explored, including paint sprays, and printer toner powders distributed on white paint. Theoretically, the correlation results are precise to ±0.02 pixels.

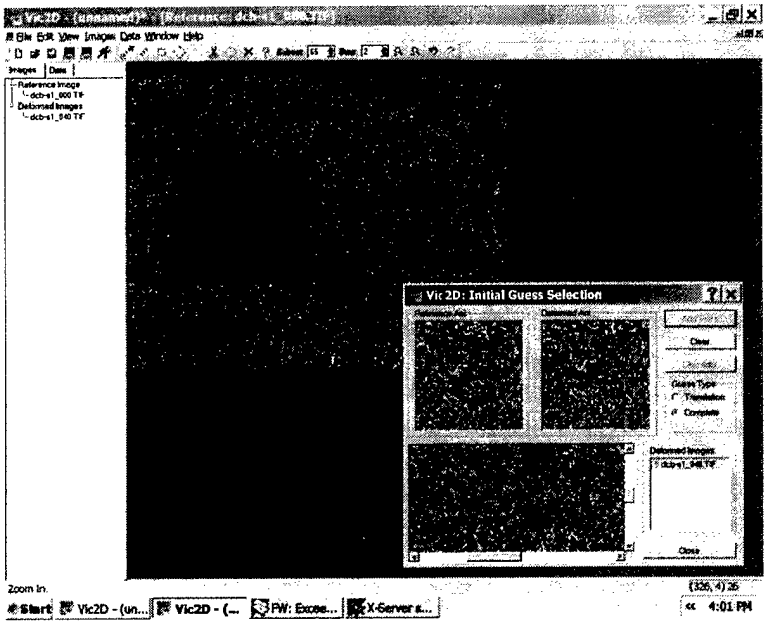

Figure 4: Screen shot of VIC2D system.

2.4 System Integration

Previous work in the group was focused on the numerical analysis of crack growth, specifically by use of the so-called cohesive zone model approach.

The new experimental capabilities have been integrated into this work, and now present an opportunity for combined numerical – experimental investigations in mechanics of materials enabling the experimental verification of numerical predictions. Figure 5 depicts an overview of the assembled experimental facility, the data flow and the integrations with the numerical analysis work. As demonstrated in Section 3.1 of this report, the strength of this approach arises since the facility allows one to compare not only the measured and predicted global specimen behavior (force – crack opening displacement – crack growth) but also the strain fields locally at the crack tip.

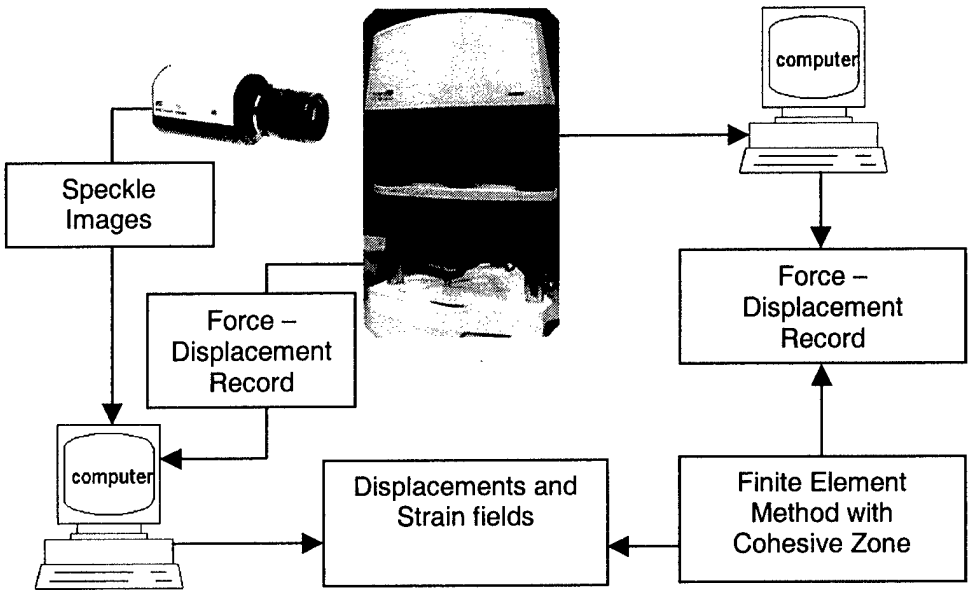

Figure 5: Assembly of experimental facility and integration with numerical analysis.

2.5 Further Equipment

In the laboratory, the following additional pieces of equipment are available:

- Machine Vision System

The MeX machine vision system is specifically designed for the 3D-surface topology reconstruction of fracture surfaces, and for the measurements of the formation and evolution of strain inhomogeneities at the surface of test specimens. 3D-surface topologies are reconstructed following principles of stereoscopy. In stereo pictures the variation of a surface elevation appears as a local shift, Δx, between corresponding points. The elevation of the surface, Δz, is than calculated by $\Delta z=\Delta x/[2M \sin(\theta/2)]$, where M is the magnification of the image. Combining this theory with a matching-algorithm fast computer based contact-less surface analysis is possible.

The machine vision system uses gray-level-based identification algorithms to locate corresponding (homologue) points in the two stereo images. The image processing program allows the creation of dense, high-quality 3D models of fracture surfaces, and their quantitative assessment from digital elevation models, see Fig. 6a for a screenshot of the "Profile Analyzer Mode". The MeX system was developed at the Institute of Solid-State Physics of the Austrian Academy of Science, Leoben, Austria, and the Institute for Computer Graphics and Vision at the Technical University Graz, Austria,

and is now commercially available from Alicona GmbH[5]. Collaboration of the PI with the above-mentioned researchers is ongoing.

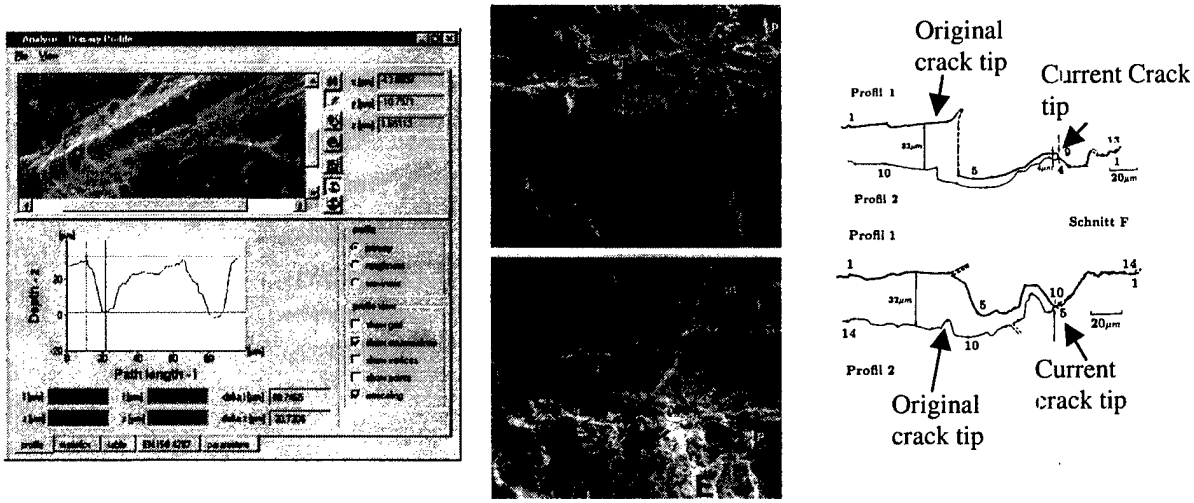

(a) (b) (c)

Figure 6: (a) A screen shot of the machine vision system showing the profiling interface. (b) Fatigue crack growth in high strength steel. Stereo-image pair of fracture surfaces after final fracture in liquid hydrogen. (c) Crack profiles as determined along matching paths E and F of the stereo image pairs.

Further equipment includes:

- Diamond band saw,
- Nikon light microscope (can be combined with the digital camera),
- Boom stand,
- Low magnification light stereo microscope,
- Cold light source with a bifurcated gooseneck light-guide,
- Specimen fixtures (three and four point bend, tension, torsion, compression).

[5] Alicona Imaging GmbH, Parkring 2, A-8074 Grambach, Graz, Austria; phone +43 316 4000 700 and fax 4000 711.

3. RESEARCH PROJECTS SUPPORTED BY THE EQUIPMENT

3.1 Crack Growth in Carbon-Carbon Composites

3.1.1 Introduction

The PI is currently leading a program on the development of functionally graded composites in the carbon-carbon system for aircraft brakes in collaboration with several Co-PIs from Purdue University, Honeywell Aircraft Landing Systems (ALS), and the National Composite Center (NCC). This program is funded by the Indiana 21st Century Research and Technology Fund. The research undertaken aims at the development of low cost advanced high temperature composites, and their use in e.g. for aircraft brake systems. Using the P4A (Programmable Power Preforming Process for Aerospace) capabilities at NCC, composite microstructures graded in fiber length, orientation, and fiber type/volume fraction are deposited in a near-net shape composite performing process at NCC, and subsequently densified at Honeywell ALS. The application of the P4A process to production of high temperature composites is novel and thus fundamental data on materials produced by this process are to be determined. More importantly, to assess the structural integrity of components made from the new composite, and to find the optimum microstructure of the composite for a given application, it is necessary to determine the crack growth resistance in dependence of location and the gradient in material properties. The low force test frame is ideally suited for the investigations of small-scale specimens obtained by sectioning the graded composite part.

Crack bridging is recognized as a major factor in the toughening of composite materials. As a crack propagates through the matrix of a composite material, it leaves intact fibers or fiber bundles behind that extend from one crack surface to the other, allowing for some amount of load transfer across the crack. In the carbon-carbon composites considered the spatial distribution of the crack bridging fibers is not uniform along the crack. Thus, if the specimen size considered is not significantly larger than the related microstructural length scales of the composite under investigation, the statistical distribution of the discrete fiber bridging events can lead to scatter in the in the experimental results on crack propagation. Combined experimental and computational efforts are under way to study these effects.

3.1.2 Methodology

Double cantilever beam (DCB) specimens, as shown in Fig. 8, were machined from pitch in-plane random fiber carbon-carbon composites with the crack plane parallel to the main reinforcement plane. To enable the use of the DCB specimen geometry, several modification to its standard form where made. Two steel layers with 0.8 mm thickness were bonded to each side of the specimen by using epoxy glue at room

temperature. The attached stiff layers allow one to avoid fracture of the specimen due to bending at the root of the DCB specimen. Furthermore, a 50% side groove, as shown in Fig 9, was introduced on one side of the specimen. This side notch keeps constrains crack growth to a path along the symmetry axis of the DCB specimen. The DCB specimens possessed an initially sharp crack (V-notch), which was cut by using thin razor blade sprinkled with the diamond-lapping compound with standard concentration. The width of the tip of the V-notch is 0.04 mm as measured by use of an optical microscope. The unnotched side surface of the DCB specimen was polished and covered with a speckle pattern to enable the subsequent measurements with the digital image correlations system. The speckle pattern was obtained by depositing a mist of white paint onto the black carbon-carbon composite. Piano hinges glued to the steel layers were used to attach the specimen to the fixtures of the mechanical test frame. Loading of the DCB specimen was performed under displacement control with a loading rate of 0.001 mm/sec.

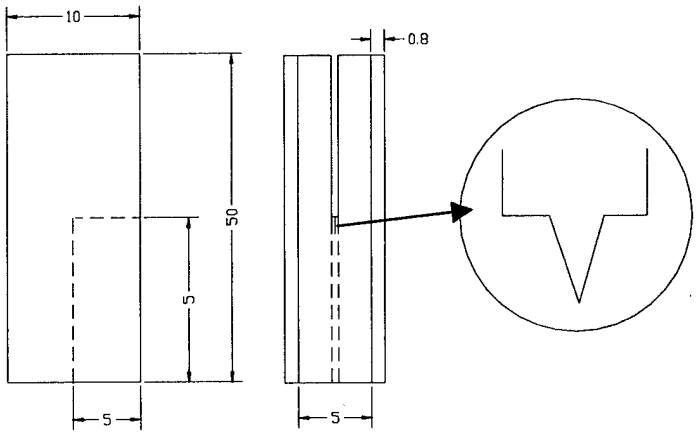

Figure 7: DCB specimen geometry.

Numerical simulations of the crack growth experiments were performed by use of the finite element method. Specifically, to account for crack growth the framework of cohesive zone elements was used. Thereby, a softening traction – separation law accounts for the material separation processes which include matrix fracture, fiber bridging and fiber failure. For the case of mode I loading as considered here, a constitutive relationship between normal traction, T_n, and the displacement jump across the crack, Δ_n, can be written as:

$$T_n = ez\sigma_{\max}\frac{\Delta_n}{\delta}\exp\left(-z\frac{\Delta_n}{\delta}\right) \tag{1}$$

with σ_{max} the cohesive strength, δ the cohesive length, Γ=9/16 $\sigma_{max}\delta$ the cohesive energy, and z=16e/9. This constitutive equation is embedded in cohesive elements located in front of the initial crack tip along a straight line. To account for the side notch, the depth

of the cohesive zone elements was taken to be 5 mm while the depth of the surrounding solids is given by the full specimen depth of 10 mm. To capture the two distinctly different processes occurring during crack growth in a composite, namely matrix fracture and failure of fibers bridging the crack behind the matrix crack tip, two separate sets of cohesive zone properties are defined for the material separation process associated with the matrix ($\sigma_{\max,m}, \delta_m$) and the fiber bridging ($\sigma_{\max,f}, \delta_f$). The tip of the matrix crack and that of the end of the bridging zone are defined by the condition that $\Delta_n=\delta_m$ or $\Delta_n=\delta_f$, respectively. In the finite element model of the DCB specimen, two cohesive zones act in parallel along the crack. All computations were performed with the software ABAQUS.

3.1.3 Results

Experimental results of a typical experiment performed in the set-up described above, are given in Fig. 8, in the form of force, F, vs. crack opening displacement, COD, and as crack extension, Δa, vs. crack opening displacement, COD. It is evident from the results in Fig. 8 that the processes associated with crack growth in the material under investigation lead to a "saw-tooth" shape in the experimentally determined F-COD data. Similarly, the crack extension data show regions in which the crack grows continuously, then is slowed down or arrests, and subsequently grows again. These effects – at least qualitatively – can be attributed to the non-uniform distribution of bridging fibers.

In the simulations the carbon-carbon composite was modeled as a linear elastic solid with E=13 Gap and ν=0.26, and for the steel layers E=207 Gap, and ν=0.3. The mesh for the crack growth studies reported in this section possessed a length for the cohesive zone elements of 0.25 mm. The investigation started by assuming a carbon matrix only specimen without any carbon fibers.

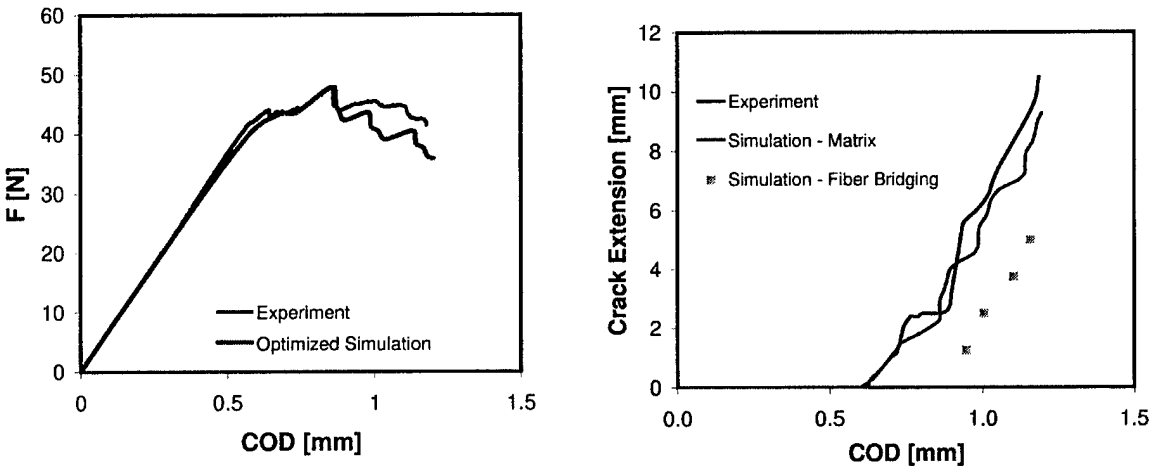

Figure 8: Results from DCB tests and simulation: (a) F-COD, (b) Δa_m vs. COD.

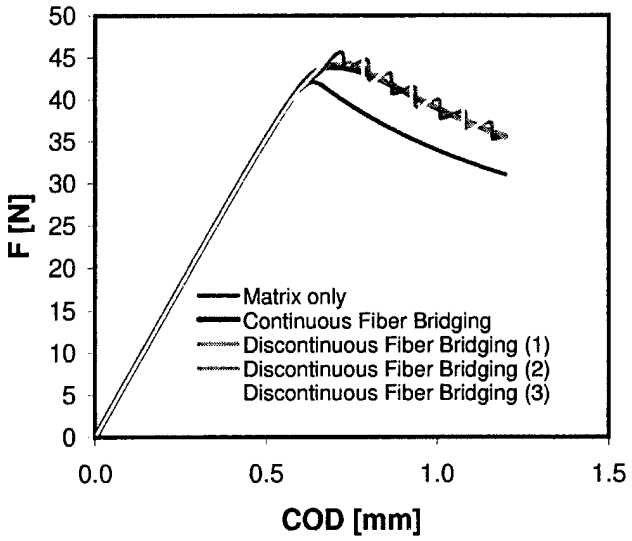

Figure 9: Simulation of DCB test, comparison of various cases in the cohesive zone parameters.

Then in the simulation, carbon matrix failure properties are assigned to all cohesive elements. The properties for the matrix failure were chosen based on toughness data for graphite, equating toughness with cohesive energy, and then choosing $\sigma_{\max,m}$, δ_m accordingly, see Table 3. The simulation of crack growth in this system leads to a *F-COD* curve at a load level quite below the experimental data. Thus, the effects of fiber bridging were accounted for in the next step. It is well recognized that the traction – separation law corresponding to crack bridging due to fibers with orientation mainly parallel to the crack growth direction is dominated by the processes of fiber pull-out, fiber bending, matrix spelling and fiber failure. While the details of these processes were not accounted for in the present study, the resulting traction separation law is characterized by low cohesive strength, but relative large cohesive length values. Initially, fiber-bridging events were assumed to occur homogeneously along the crack path, and a second set of cohesive zone elements was located in parallel to the one characterizing the matrix. Various parameter sets were investigated in a trail-and-error process, and the parameter set approximating the experimental data best is represented in Table 2, with the computed *F-COD* data given in Fig. 8. Accounting for the bridging events obviously increases the load level, and aligns the simulation results better with the experimental data. Nevertheless, the predicted *F-COD* data is smooth and crack extension is a continuous process. To simulate the interaction of the continuous matrix crack growth with the spatially discrete fiber bridging, the cohesive zone locations accounting for bridging were then distributed only at certain spots along the assumed crack path. Three such cases were investigated, with the specific data given in Table 2. In all cases, matrix only conditions were assumed for the first 1 mm of crack extension. After that, cohesive elements representing fiber bridging were located at intervals 0.75, 1.25, and 2.5 mm, respectively. The cohesive zone parameters for these cases were chosen such that the total energy spent in the fiber bridging events along the crack path was equal to that in the case of the continuous distribution. To accomplish this, the cohesive strength was increased while the cohesive length was kept constant.

Results from the simulations performed with the discontinuous fiber bridging distribution are given in Fig. 9. For all three cases, the simulations well predict a "saw-tooth" type *F-COD* curve, with the amplitude of individual peaks and the distance between individual peaks increasing as the distance between fiber bridges becomes wider and the strength of the individual bridging events increases.

While the results in Fig. 9 already show trends similar to those observed in the experimental *F-COD* data, an attempt was made to more closely approximate the experimental data by use of a

	Cohesive Strength [MPa]	Cohesive Length [mm]	Distance between bridging zones [mm]
Matrix only	$\sigma_{\max,m} = 50$	$\delta_m = 0.01$	-
Continuous bridging	$\sigma_{\max,f} = 2$	$\delta_f = 0.05$	0.00
Case (1)	$\sigma_{\max,f} = 12$	$\delta_f = 0.025$	0.75
Case (2)	$\sigma_{\max,f} = 20$	$\delta_f = 0.025$	1.25
Case (3)	$\sigma_{\max,f} = 40$	$\delta_f = 0.025$	2.50

Table 3: Cohesive zone parameters used in the simulation of the carbon-carbon composite.

Combination of crack bridging events described a varying the cohesive zone parameters. The best approximation between model prediction and experimental results was obtained by combining the following sequences of crack bridging cohesive zone elements: $\sigma_{\max,f} = 10$ MPa, $\delta_f = 0.05$ mm, first bridging event after 1 mm over a length of 0.25mm, plus bridging events with $\sigma_{\max,f} = 25$ MPa, $\delta_f = 0.03$ mm, after 2.25 mm over a length of 0.25 mm, and with $\sigma_{\max,f} = 15$ MPa, $\delta_f = 0.03$ mm, after 4.75 mm and 7.25 mm over a length of 0.25 mm each. The results of this optimized simulation are given together with the experimental data in Figure 8. Good agreement between experimental and simulated *F-COD* data were obtained, especially *COD*<0.8 mm. Overall, the predicted extension of the matrix crack tip compares well with experimental data, however, the individual crack arrest – renucleation events could not be captured in detail. While in the experiments the location of the location characterizing the fiber bridging break down is difficult to determine in the present material, the simulation show that this event occurs with a considerable delay relative to the matrix crack tip. The break down of the first fiber bridging location at Δa=1 mm occurs at *COD*=0.95 mm, at this instance of loading the matrix crack has already propagated 5.7 mm.

As demonstrated in the previous paragraphs, good agreement between the experimental and numerical data for the crack growth simulation has been obtained. Nevertheless, both *F-COD* and Δa-*COD* data represent the global specimen behavior. The question remains on how accurate the computations predict the state of the specimen locally at the crack tip during crack growth. To investigate this aspect, the digital image correlation method was applied to obtain the strain fields at the crack tip for a growth crack. A digital picture taken at zero load was compared to a digital picture taken at an extension of the matrix crack of 4 mm. The experimentally determined distribution of ε_{22}

in front of the crack is given in Figure 10. Figure 11 depicts the computed strain fields, obtain for $\sigma_{max,m}$=50 MPa and δ_m=0.01 mm as used in the simulations described in the previous section and for $\sigma_{max,m}$=150 MPa and δ_m=0.0033 mm. For these computations finite element meshes with the smallest element size of 0.025 mm were used. Form a comparison between Fig. 10 and Fig. 11a it is evident that the strain fields predicted with $\sigma_{max,m}$=50 MPa do not compare well with the experimentally measured strains, despite the fact that the crack growth behavior was well approximated. Much better agreement between the strain fields from experiment and simulation was obtained in the case of $\sigma_{max,m}$=150 MPa, see a comparison between Fig. 10 and Fig. 11b.

3.1.5 Conclusion

Crack growth in a carbon-carbon composite with bridging fibers has been studied both experimentally, as well as with the finite element method. The simulation employ the cohesive zone model approach to account for crack growth in the matrix, as well as for the bridging effects due to the presence of fibers. By accounting for non-uniform distributions of the crack bridging events the global specimen response in terms of *F-COD* and Δa-*COD* was well represented. Detailed investigations of the crack tip strain fields with the digital image correlation method however, show that the choice of cohesive zone parameters has to be performed carefully. For parameters allowing a good approximation of the global specimen response the crack tip strain fields can be predicted qualitatively correct, but quantitative agreement in strain fields and global specimen response it thereby not assured.

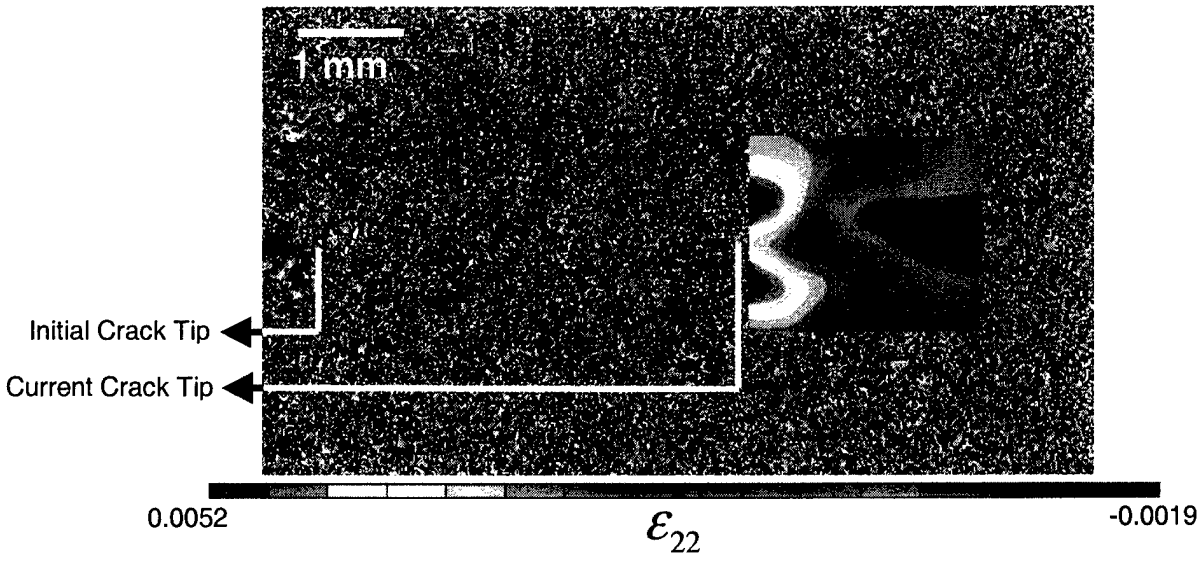

Figure 10: Experimentally determined ε_{22} field for a growing crack in the C-C composite.

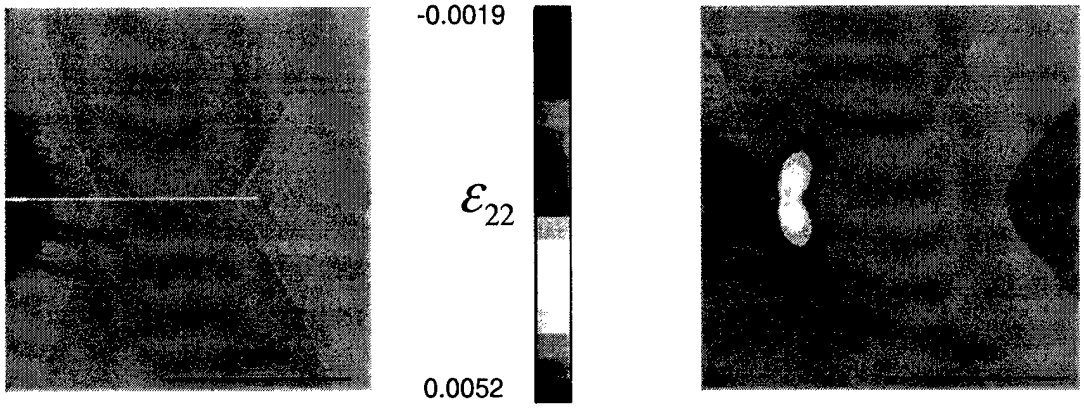

(a) (b)

Figure 11: Numerically predicted ε_{22} field for a growing crack in the C-C composite: (a) $\sigma_{max,m}$=50 MPa, (b) $\sigma_{max,m}$=150 MPa.

3.2 Properties of Porous Thermoplastic Vulcanizates

3.2.1 Introduction

Thermoplastic vulcanizates (TPVs) are a special class of thermoplastic elastomers, which use the synergistic interactions of an elastomer-thermoplastic polymer blend. These materials are attractive since they are amenable to fabrication into parts using the rapid techniques used for thermoplastic materials such as blow molding, injection molding, and extrusion. Conventional thermoset elastomers have been widely used for the suppression of sound and vibration, and in many situations foamed elastomers are advantageous in that they allow substantial weight savings over solid materials, and are largely compliant deformation needed in sealing application. For successful applications of TPVs to such places, dynamic mechanical properties of foamed TPVs are required, and it is desirable to establish a relationship between the properties of the material and the void fraction. The results on the viscoelastic properties of foamed TPV materials reported here were obtained during a research project sponsored by Ford Motor Company and Advanced Elastomer Systems, Akron, OH. The goal of the research project was to obtain an understanding of the behavior of foamed TPV materials in door sealing applications in automotive systems.

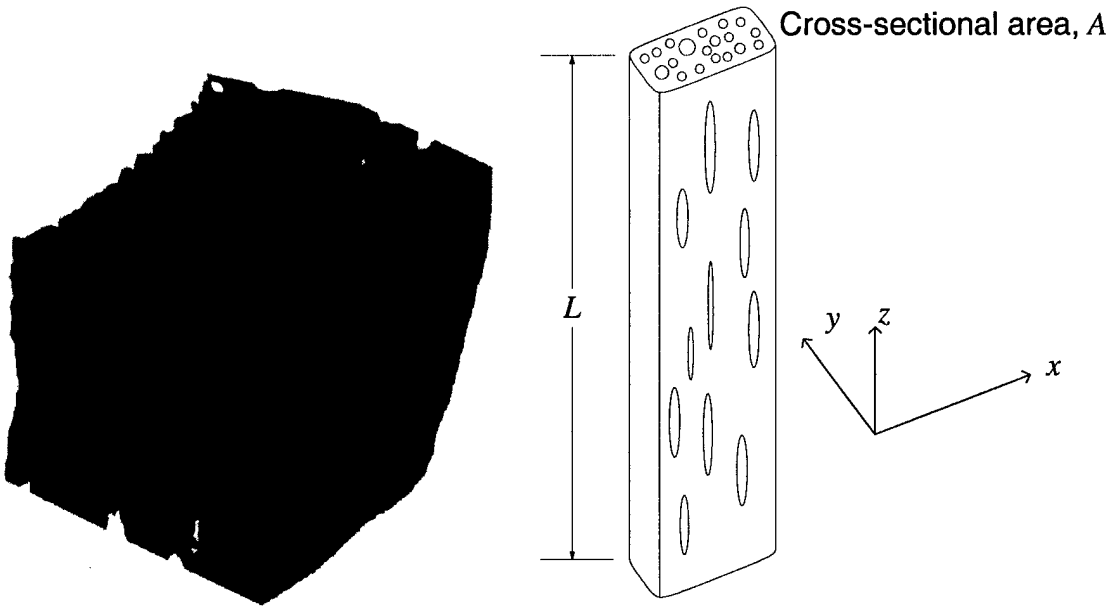

Figure 12: (a) Microstructure of TPV foam, density 630 kg/m^3; (b) Schematic of anisotropy and coordinate system.

Water foamed and extruded samples of Santroprene® rubber 121-68W228 were investigated. All samples were foamed from a solid elastomer with a density of ρ_0=980 kg/m^3, and densities in the range from ρ=250 kg/m^3 to the full dense specimen were investigated. A sample microstructure are given in Figure 12a, showing that the resultant foam is a combination of open and closed cells. Figure 12b shows the schematic of the extruded samples and the coordinate system.

Two groups of measurements were performed:

(1) In an enhanced "resonance" method rod-like specimen were excited by a shaker at one end. The longitudinal acceleration was measured at both ends using accelerometers. The elastic modulus and the loss factor of the sample were calculated from the measured transfer function between the two accelerometer signals. A similar method was used by to measure the complex moduli of acoustic materials. The resonance method was adopted as an ANSI standard (ANSI S2.22-1998). The frequency dependent longitudinal elastic modulus and loss factor were measured in the frequency range from 500 Hz to 4 kHz.

(2) Relaxation tests were conducted in the ELF 3200 test frame under axial loading for both in longitudinal and the transverse direction. Furthermore, torsion test were conducted to measure the instantaneous in-plane shear modulus as well as the torsion relaxation behavior.

The predictions from the resonance method experiments and the relaxation tests are compared to each other, and micromechanical models are used to further analyze the experimental data.

3.2.2 Properties of Foamed TPVs - Analysis

The mechanical properties of the foamed samples were anisotropic due to the extrusion process. The stiffness in the extrusion direction was observed to be much larger than that in the other directions. A transverse isotropic material description may thus be used to characterize the deformation characteristics of the foamed TPVs. In this case, five independent elastic constants are required. Here, the longitudinal and transverse Young's moduli, E, E', and G', the in-plane shear modulus have been determined experimentally.

In the following, the complex and relaxation moduli are defined and the relationship between the two is described. Identical procedures apply to the complex and relaxation moduli both in the plane of transverse isotropy and in the direction normal to it, as well as for the shear modulus.

A commonly accepted method to model the dissipation of vibration energy is to use complex elastic moduli for the dynamic properties of solids. For uniaxial vibrations in the z-direction ($\hat{\sigma}_x = \hat{\sigma}_y = 0$) the complex modulus is defined as,

$$\hat{E}(\omega) = \frac{\hat{\sigma}_z(\omega)}{\hat{\varepsilon}_z(\omega)} = E_d(\omega) + jE_l(\omega) = E_d(\omega)\left[1 + j\eta(\omega)\right], \tag{2}$$

where E_d and E_l are the dynamic and loss moduli, respectively, and η is the loss factor. The Fourier transforms of stress and the strain are defined as $\hat{\sigma}_z(\omega) = \int_{-\infty}^{\infty} \sigma_z(t) e^{-j\omega t} dt$ and $\hat{\varepsilon}_z(\omega) = \int_{-\infty}^{\infty} \varepsilon_z(t) e^{-j\omega t} dt$. With the assumption that the dynamic properties do not exhibit resonance-like frequency dependences, the dynamic modulus was approximated as:

$$E_d(\omega) = C_d \omega^{\frac{2\eta}{\pi}}, \tag{3}$$

where C_d is a constant determining the frequency dependence of the dynamic modulus. In this equation, the static modulus was assumed to be negligibly smaller than the dynamic modulus.

The frequency dependence of the material properties can be inferred from relaxation tests. In a relaxation test, a strain step function with a magnitude ε_0 is imposed to the material, and the resulting time-varying stress is measured. The relaxation modulus, $E_r(t) = \sigma_r(t)/\varepsilon_0$, is related to the dynamic modulus as

$$E_d(\omega) = \omega \int_{-\infty}^{\infty} E_r(t) \sin \omega t dt \tag{4}$$

The time dependence of the relaxation modulus can be derived from the frequency dependence of the dynamic modulus and equation (3) as:

$$E_r(t) = C_r t^{-\frac{2\eta}{\pi}} = \frac{C_d}{2\Gamma\left(1-\frac{2\eta}{\pi}\right)\sin\left(\frac{\pi-2\eta}{2}\right)} t^{-\frac{2\eta}{\pi}} \tag{5}$$

where Γ is the Gamma function. Thus, the ratio between the two material constants, C_r and C_d, is $2\Gamma(1-2\eta/\pi)\sin[(\pi-2\eta)/2]$=2.5.

The influence of the void fraction on the mechanical properties of porous or foamed materials has been the subject of previous investigations, and several micromechanical models have been proposed, mainly under the assumption that the matrix (solid TPVs in the present case) is isotropic. Micromechanical models assuming a TPV matrix with voids can assumed to be valid because the cross-linked rubber particles are less than 2 μm in diameter, which is much smaller than the size of the voids.

3.2.3 Axial Loading

If the voids are spheroidal with aspect ratio *l/d*, the resulting material properties of the foamed TPV are anisotropic. This anisotropy can be taken into account using the Eshelby tensor within the Mori-Tanaka's (MT) method. The longitudinal and transverse elastic moduli of the foamed TPVs can then be estimated using the relations:

$$\frac{E}{E_0} = \left[1+\phi\frac{(A_1+2\nu_0 A_2)}{A_0}\right]^{-1},$$

$$\frac{E'}{E_0} = \left[1+\phi\frac{\left[-2\nu_0 A_3+(1-\nu_0)A_4+(1+\nu_0)A_5 A_0\right]}{2A_0}\right]^{-1} \tag{6 a,b}$$

where E_0 and ν_0 are Young's modulus and Poisson's ratio of the solid, un-foamed elastomer, and ϕ=1-ρ/ρ_0 is the void fraction with . The procedures for the calculation of the constants, A_i, and Eshelby's tensor are found in papers by Tandon and Weng. As discussed later, the loss factor was not affected by the voids and remained constant with the void fraction. This suggests that the relation shown in equation (5) can be used to determine both the complex dynamic and the relaxation modulus.

Figure 13 shows the longitudinal elastic modulus and the loss factor of the six samples investigated with the resonance method. The frequency dependence of the elastic modulus is linear in the log-log plot, except at the instance of anti-resonances. There, the measured elastic modulus are affected by large experimental error related to limited dynamic range of accelerometers and too small phase difference between two accelerometers.

The scattering of acoustic waves from individual voids can be enhanced the damping in foams. The lowest frequency at which resonant scattering effects within the voids affect the mechanical properties of the foam is

$$\omega_{res} = \frac{2}{d_{void}} c_L , \tag{7}$$

where ω_{res} is the resonance frequency of the void cavity of radius d_{void} and c_L is the longitudinal wave speed in the solid. For the foams under study, the largest void diameter was approximately 0.4 mm. The corresponding resonance frequency is thus 320 kHz, which is much greater than the frequency range of interest.

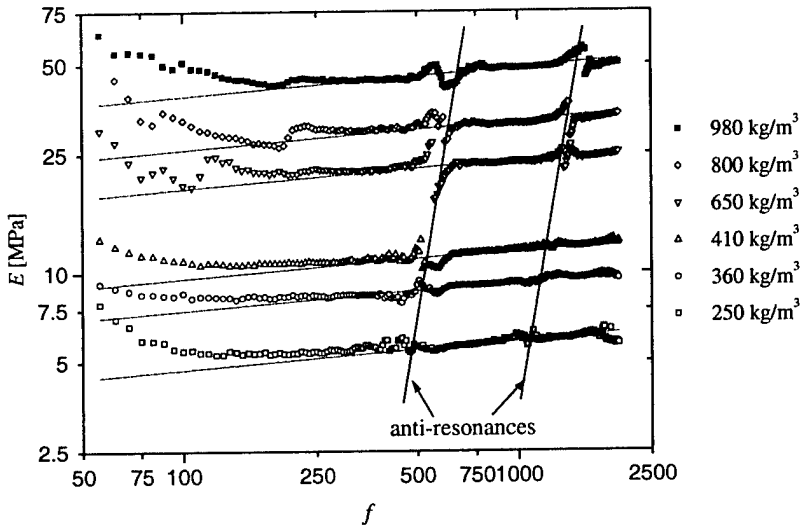

(a)

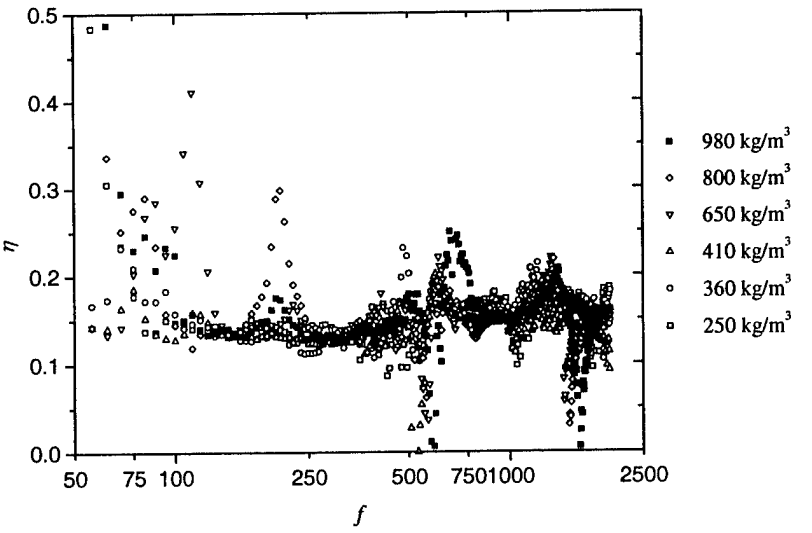

(b)

Figure 13: Viscoelastic properties of the elastomer made of TPV measured using the resonance method. (a) Dynamic modulus and (b) loss factor.

Thus, resonant scattering effects did not contribute significantly, and most of the dissipation of vibration energy was caused by the material damping. Consequently, the loss factor, η, is expected to be independent of the relative density. This is confirmed by the experimental results shown in Figure 13(b). The measured loss factor is approximately constant, equal to 0.15, regardless of relative density and frequency. From the measured loss factor, the exponent in equation (2) is given as $2\times0.15/\pi = 0.0955$.

To estimate the constants, C_d, in equation (2), the measured frequency dependence of elastic modulus was interpolated by straight line with given slope, $2\eta/\pi$, in log-log scale as shown in Figure 13(a). To minimize the effects from the experimental error, the data near anti-resonance was excluded in the interpolation. The interpolated frequency dependence of the dynamic modulus is shown as straight lines in Figure 13(a). The estimated value of C_d for the six TPV materials is shown in Table 4. The results show that the variation of the elastic modulus as a function of the relative density (or void fraction) did not depend on frequency within the frequency range of interest.

ρ [kg/m^3]	C_d [MPa]	C_r [MPa]	$C_r^{'}$ [MPa]	C_d / C_r
250	3.03	1.3	0.1	2.3
360	4.8	1.9	0.4	2.5
410	6.16	3.1	0.9	2.0
650	12.34	5.9	2.5	2.1
800	16.64	7.2	4.8	2.3
980	25.2	10.4	8.8	2.4

Table 4: Material constants for TPV samples.

Since the experimental method based on one-dimensional longitudinal wave propagation requires elongated or rod-shaped samples, and this method can only be used to obtain properties in the longitudinal direction. In cases where the samples are extruded, however, the voids are not necessarily symmetric, and the material properties are anisotropic. To investigate the anisotropy of the foamed TPVs under investigation, the relaxation modulus was measured in compression tests using the ELF 3200. The step displacement of 1 mm was imposed as initial conditions and the time-dependent relaxation modulus was measured. Figure 14 shows the measured relaxation curves of the sample along x- and z- directions.

The measured relaxation modulus was interpolated using the relationship shown in equation (5) following the same numerical procedures used for interpolating the dynamic modulus. Estimated values for the material constants for the longitudinal and transverse directions of the TPV materials, C_r, $C_r^{'}$ are shown in Table 4. In the time period used in this experiments, the relaxation modulus followed very closely the relationship shown in equation (5). Table 4 also shows the measured ratio, C_d/C_r. The measured ratio is closely similar to the estimated ratio from equations (5) as $2\Gamma(1-2\eta/\pi)\sin\left[(\pi-2\eta)/2\right]=2.5$.

The results shows that the frequency- and time-dependency shown equations (2) and (5) represents the viscoelastic properties of TPVs in the current frequency and time range of interests. The experimental data for the TPV foams, discussed in previous sections, suggest that the dynamic modulus varies with the void fraction, and does not depend on frequency.

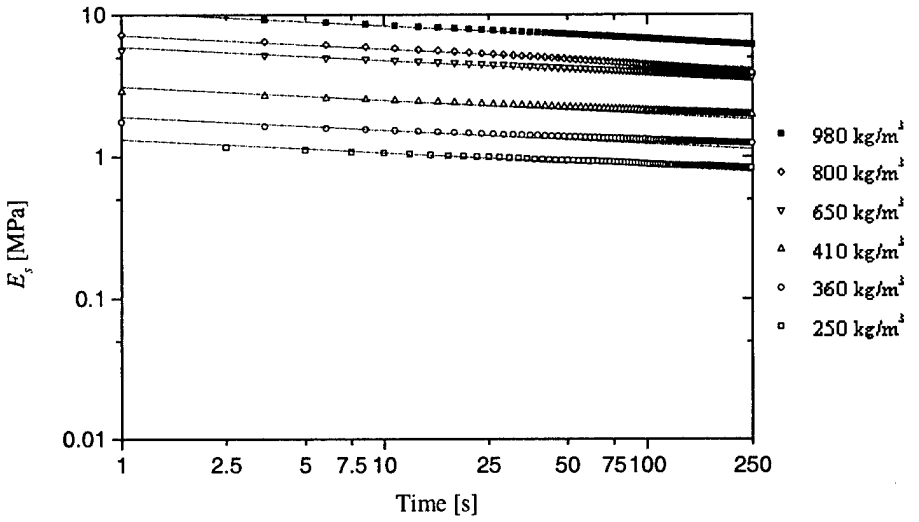

(a)

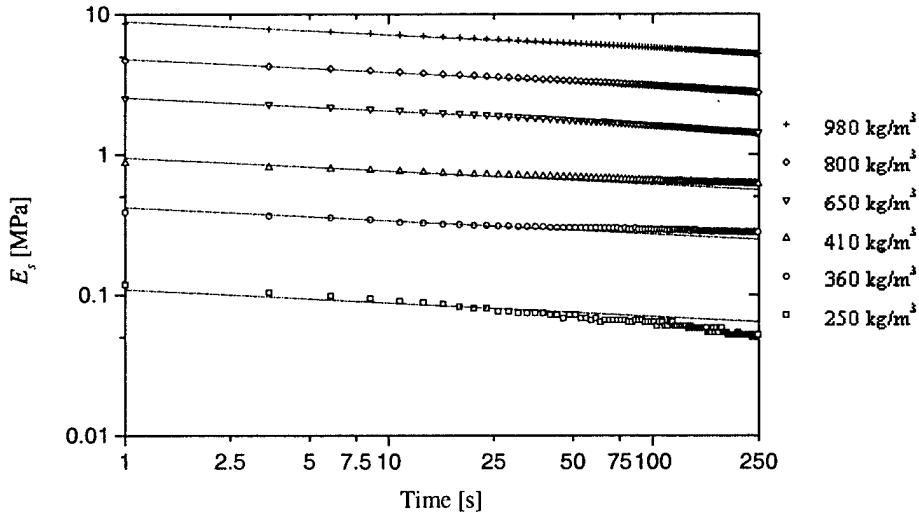

(b)

Figure 14: Uniaxial relaxation modulus measured for the six TPV samples. (a) z-direction and (b) x-direction.

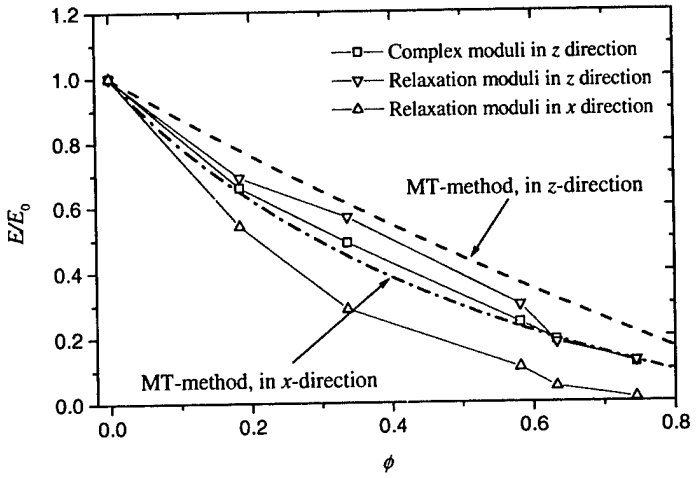

(a)

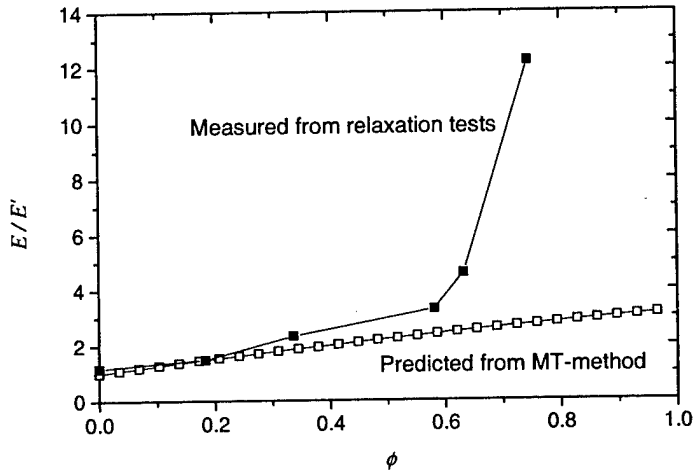

(b)

Figure 15: (a) Measured variations of material constants f_v with relative density for TPE elastomer and comparison with the predictions from generalized self consistent model. (b) Measured and predicted ratio E/E', and its dependence on the void fraction.

Thus, the expression for the dynamic modulus, in equation (2), can be rewritten as

$$E_d = C_{d0}\omega^{\frac{2\eta}{\pi}} f_v(\phi), \tag{8}$$

where C_{d0} is the material constant measured for the solid, unfoamed elastomer and f_v is a function that describes the dependence of the elastic modulus on the void fraction. f_v can be estimated also from the measured relaxation modulus. A similar expression can be written for the elastic modulus in transverse direction, thus allowing for the determination

of the dynamic modulus even in specimen directions for which long rod-like specimens are not available.

Figure 15(a) shows the measured variation of f_v with the void fraction together with the predictions from equation (6). To take account the spheroidal void shapes, the MT-method described in the previous section was used with $l/d = 3$. The MT-method predicts elastic moduli that are greater than the measured dynamic moduli. Figure 15(b) shows variation of the measured and predicted ratio, E/E', with void fractions. The measured ratio, E/E', increases more rapidly than the predicted vales from the MT-method. The possible reason for the discrepancies between the predictions and the experimental data is the irregular shape of the voids (Figure 1). Obviously, the shape of the voids is not spheroidal. The voids are connected to each other in some cases, which is generally not taken into account in any MT-method. These phenomena become more important as the void fraction increases, as becomes the potential for anisotropic matrix properties resulting due to the water foaming process at high void volume fractions.

3.2.3 Torsion Tests

Torsion tests were performed with the capabilities of the ELF 3200 system on extruded tube specimens of the TPV. The specimen set-up is depicted in Figure 1.

Again, micromechanical models were used to compare experiments and predictions. With the Mori-Tanaka (MT) method following Tandon and Weng the shear modulus is:

$$\frac{G_s}{G_0} = 1 + \frac{1+\phi}{-1+2\phi A_{12}} \tag{9}$$

where A_{12} is a component of the Eshelby's tensor. Furthermore, predictions from the dilute approximation and the linear rule of mixtures were evaluated.

In a first step the instantaneous shear modulus was investigated. To this end, the material property of the solid elastomer was obtained as $G_0 = 3.4$ MPa, by use of data from the compression tests, and assuming a Poisson's ratio of $\nu_0 = 0.45$. The instantaneous shear modulus was determined from measured torque-twist curves and data is depicted together with the micromechanical model prediction in Figure 16. Good agreement between the experimental data and the model predictions is observed.

Subsequently, torsion relaxation test were performed to determine the loss factor of the TPV materials. Following equation (5), a dependence of the relaxation modulus on time was assumed as follows:

$$G_s' = C_s t^{-(2\eta/\pi)}, \tag{10}$$

Here, C_s now is a material constant for in-plane shear, and again from the theoretical results the loss factor does not depend on the relative density of the material.

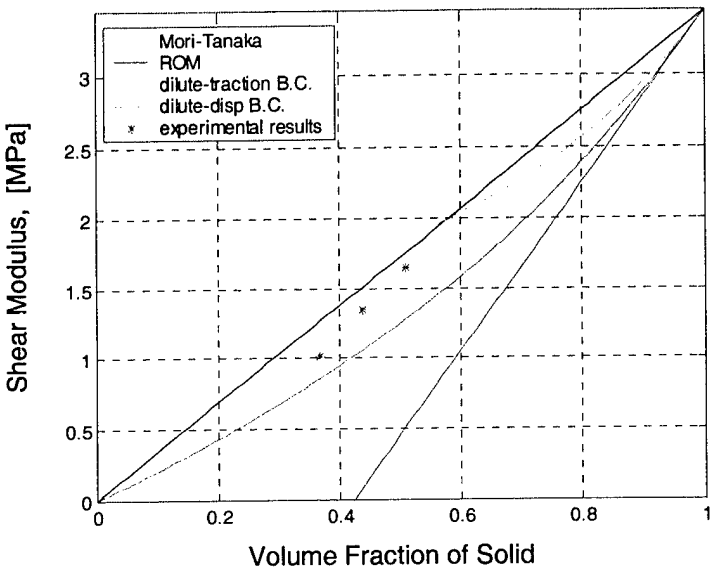

Figure 16: Shear modulus of TPV in dependence of volume fraction.

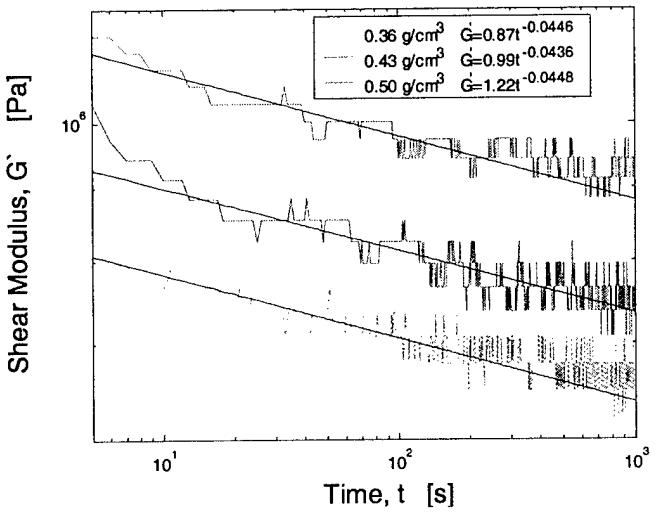

Figure 17: The variation of shear modulus with time in the relaxation test for TPE with different densities.

Figure 17 depicts the shear modulus versus time in log-log scale. Again, a power relation between the shear modulus and time is obtained. As shown in the figure the three lines are almost parallel to each other, thus a loss factor independent of void volume fraction can be obtained as $\eta = 0.044 \times \pi / 2 = 0.07$. Due to the reduced force resolution of the torque load cell as compared to the axial load cell, less confidence can be placed in the experimental data from the torsion test.

3.2.4 Conclusion

The viscoelastic properties of foamed TPVs were measured using two different methods. The frequency-dependent dynamic and loss moduli were measured using the resonance method. Time-dependent relaxation moduli were measured in the relaxation tests both for axial loading as well as for torsion. The ELF 3200 system proved itself as well suited for this task, in the axial loading set-up. For the torsion experiments the resolution of the load cell was not sufficient enough to provide accurate measurements. The torsion tests are currently repeated with shorter specimens, which will lead to larger torque values.

3.3 Ongoing Research

(1) Work continues on carbon-carbon composites. While past studies (section 3.1) were performed on currently commercially available carbon-carbon composite materials used in aircraft brakes, the investigation is now shifting towards the analysis of the functionally graded materials as these become available after being produced and processed at the industrial project partners. In addition to the fracture tests already initiated, it is planned to perform tests on individual carbon fibers in the unprocessed and processed condition, in order to aid in the strength prediction of these composites

(2) Investigation on polyurethane seating foams will be conducted in collaboration with other faculty (A. Bajaj and P. Davies) from the School of Mechanical Engineering. Similarly to the work on TPV, the time dependent properties of seating foams for the automotive industry are being investigated with the ELF 3200.

(3) Torsion failure of viscoelastic (tissue) material is studies in collaboration with R. Chan (Department of Speech and Audiology at Purdue University). In this project, studies of failure of focal foal tissue under torsion loading have been initiated. Parallel to the tissue experiments conducted in Dr. Chan's lab, the torsion capability of the ELF 3200 will be used to study rate dependent torsion failure of gelatine like materials. Again, the experimental work will be combined with computational failure modeling.

(4) Investigations of fatigue crack growth in multiplayer structures as occurring along metal-ceramic interfaces of e.g. MEMS systems were described an a proposal to AFOSR.

4. CONTRIBUTION TO TEACHING

Two graduate students have been working with the equipment supported by this grant. Junhong Park (PhD, 2002) performed the work on the TPV material, and Jibin Han (PhD candidate) continues to work on the carbon-carbon composite materials.

The PI teaches a course on "Micromechanics of Materials" on the graduate level within the School of Mechanical Engineering at Purdue. During the Spring 2002 semester three graduate students performed their course projects with the use of the equipment supported by the equipment grant. The following projects were conducted:

1. Investigation of the Mechanical Properties of a Polymeric Packaging Foam
   Closed cell foam specimens were tested in compression under various strain rates, and the measured properties were compared to those of a corresponding open cell foam obtained by punching the closed cell foam with a fine needle. The contribution of the gas contained in the cells to the foam response was determined and compared to analystical results.

2. Investigation of a Honeycomb Panel Core Material
   Compression tests were conducted on a Nomex honeycomb core material are used in sandwich panels. While tensile tests on the paper based honeycomb wall material are difficult due to problems in specimen preparation, an invesrse method was devised to obtain the honeycomb properties by comparing experimental data and predictions from beam models.

3. Compression Tests on TPV Samples
   Compression tests on TPV samples as described in the previous section of the report were repeated. Measured instantaneous Young's moduli were compared to micromechanical models.

6. RELATED PROPOSALS UNDER REVIEW

Numerical Simulation and Experiments of Fatigue Crack Growth in Multilayer Structures
(Role: PI, submitted to AFOSR in response to the BAA 2002)

Statement of Relevance: Multi-layer structures dominate the design of many MEMS and microelectronic devices. To advance promising MEMS devices into field applications and to increase the reliability of integrated circuit interconnect structures, systematic studies of failure mechanisms are important. Specifically, within the proposed study the issue of fatigue crack growth is addressed. The relevance of the proposed research arises as conventional fatigue crack growth analysis methodologies based on the Paris equation

loose their validity at small scales. As the cyclic and monotonic plastic zones become of size similar to the thickness of individual layers, constraint effect become important, and the transferability of fatigue crack growth data is lost. To enable the design of reliable small-scale devices a new approach for the analysis of fatigue crack growth needs to be established. The proposed research will aid the Air Force in its developments of new small-scale devices ranging from reliable microprocessors to pressure sensors and flow control systems for use in intelligent and active aerospace components and munitions systems, to future active micropropulsion systems. To transition the research results into Air Force relevant activities and applications, the PI is actively pursuing interaction with AFRL at Eglin and with a corporate development group, to analyze failure events in actual devices and to develop potential new design guidelines.

Objective of Research: The goal of the proposed research is to undertake a combined numerical and experimental investigation of fatigue crack growth at small scales. The proposed research aims to provide experimental evidence for constraint effects in fatigue crack growth at small scales, to develop a fatigue crack growth analysis method applicable at small scales, and to establish a framework that enables the design of small-scale devices against fatigue crack growth.

Approach: For the computational prediction of fatigue crack growth an irreversible cohesive zone model describing material separation under cyclic loading is introduced. This model relates the cyclic material separation to the tractions across the crack tip. This approach is promising for the investigation of fatigue crack growth under constraint as energy dissipation due to the formation of new crack surface and cyclic plastic deformation is accounted for independently. Experimental studies of fatigue crack growth will be performed on a MEMS relevant material system where aluminum thin films are sandwiched between two elastic substrates, and a well-defined interface is introduced. We will determine the dependence of fatigue crack growth rates on the aluminum film thickness under constant amplitude loading. Variable amplitude loading cases will be investigated for selected specimens. Cyclic in-situ loading experiments will be performed within an atomic force microscope to measure crack opening profiles and crack tip strain fields. From comparison between the crack opening profiles and strain fields computed for an ideal elastic solid, and the measured values of crack opening and strain, the parameters of the cohesive law will be determined such that simulations of fatigue crack growth under constant and variable amplitude loading can be performed.

Scientific Merit: Due to the novelties in the material combinations, and the small size of the characteristic geometric features, experimental fatigue crack growth data on multi-layer structures as of interest to MEMS have rarely been performed in the past. The use of in-situ fatigue crack tip studies in the atomic force microscope will establish measurement protocols crucial for the proper identification of cyclic material degradation. Even more important is the development and application of new fatigue crack growth analysis methods. The proposed computational method base on an irreversible cohesive zone model will for the first time allow for the quantitative investigation of the effects of constraint effects in fatigue at small scales.

7. PUBLICATIONS

A Combined Experimental-Numerical Investigation of Crack Growth in C-C Composites
(To be presented at the American Society for Composites – 2002; 17th Annual Technical Conference, journal paper in preparation for "Carbon")
J. Han, T. Siegmund

See section 3.1 for an overview of this work

Viscoelastic Properties Of Foamed Thermoplastic Vulcanizates And Its Dependence On Void Fraction
(journal manuscript in preparation for "Cellular Polymers")
J. Park, T. Siegmund, L. Mongeau

See section 3.2 for an overview of this work

Fracture Initiation And Crack Growth – Cohesive Zone Modeling And Stereoscopic Measurements
(journal manuscript in preparation for "International Journal of Fracture", a short version of the paper has been published in the proceedings of the 10th International Conference of Fracture, 2001)

C.R. Chen[a], I. Scheider[b], T. Siegmund[c], A. Tatschl[d], O. Kolednik[d], F.D. Fischer[a]
[a]Institute of Mechanics, Montanuniversität, A - 8700 Leoben, Austria
[b]GKSS Forschungszentrum Geesthacht GmbH, D - 21502 Geesthacht, Germany
[c]School of Mechanical Engineering, Purdue University, West Lafayette, IN 47907, USA
[d]Erich Schmid Institute of Materials Science, Austrian Academy of Sciences, A - 8700 Leoben, Austria

Abstract
The purpose of this paper is to study the application of a cohesive zone model, which is appropriate for the use with 3D-elements, for the numerical simulation of the crack growth in a Compact Tension specimen made of a mild steel. The main problem is how the two parameters which control the crack growth in the model, the cohesive energy G_0 and the cohesive strength T_{max}, can be determined. A procedure is proposed to determine the variation of the parameters along the crack front, $G_0(z)$ and $T_{max}(z)$, by using the local crack growth data in the specimen center and at the side surfaces and 2D modeling under plane strain and plane stress conditions, as well as the measurement of the variation of the critical crack tip opening displacement, $COD_i(z)$, along the crack front. The comparison between the experimental data and the numerical simulation reveals that the parameters of the cohesive zone model change during (the first stages of) crack extension.